



Boosting full-spectrum light driven surface lattice oxygen activation of ZnMn_2O_4 by facet engineering for highly efficient photothermal mineralization of toluene

Qiang Cheng, Yuan Li, Zhuangzhuang Wang, Xiaotian Wang, Gaoke Zhang^{*}

Hubei Key Laboratory of Mineral Resources Processing and Environment, Shenzhen Research Institute, State Key Laboratory of Silicate Materials for Architectures, Wuhan University of Technology, 122 Luoshi Road, Wuhan 430070, People's Republic of China

ARTICLE INFO

Keywords:

Surface lattice oxygen
Face engineering
Photothermal oxidation
 ZnMn_2O_4
Toluene mineralization

ABSTRACT

To improve the catalytic activity of photothermal catalysts for efficient mineralization of volatile organic compounds still keeps challenge. Herein, ZnMn_2O_4 with controllably exposed {010} facets (ZMO-H), {11-1} facets (ZMO-R), and {1-1-1} facets (ZMO-C) were firstly synthesized and used to unveil an essential role of facet-dependent activation of surface lattice oxygen for toluene mineralization under full-spectrum light irradiation. The experimental studies and theoretical calculations together evidenced that as compared to ZMO-R and ZMO-C, ZMO-H is favorable for activating surface lattice oxygen, owing to its relatively stronger light absorption, higher surface lattice oxygen content, and lower oxygen dissociation energy. The theoretical calculations further confirmed that toluene is more easily adsorbed by ZMO-H than by ZMO-R and ZMO-C. All these advantages have substantially afforded the toluene photothermal oxidation activity of ZMO-H. This finding confirms that surface lattice oxygen activation of catalyst by facet engineering is crucial on the photothermal oxidation of toluene.

1. Introduction

The surface lattice oxygen activation of catalysts plays a significant role on the efficiency of a redox reaction. For example, the reversible and highly active properties of surface lattice oxygen are widely applied to the oxygen evolution reaction [1], rechargeable metal-air batteries [2], electrochemical sensors [3], and catalytic combustion in volatile organic compounds (VOCs) [4–6]. Despite these numerous application fields, the chemically inertness of the surface lattice oxygen restricts its important role in catalytic reaction. Hence, some effective methods should be proposed to enhance the activation of surface lattice oxygen.

Common strategies for enhancing the activity of surface lattice oxygen involve cation or oxygen defect engineering [7], element doping [8,9], tuning the electron-transfer at the interface of composites [10], and surface modification of single catalyst [11]. One of the promising activation methods involves controlling the exposed facets of the catalyst, where the dominated exposed facets can optimize the hybridization of the metal-oxygen bond via regulation synthesis condition of catalyst [12]. Wei et al. reported that CeO_2 with different exposed facets have distinct surface lattice oxygen distribution and the surface lattice oxygen

played an important role in toluene combustion [13]. Ji et al. recently demonstrated that Co_3O_4 catalysts with exposed {220} facets are highly efficient for removal of VOCs due to its rich surface lattice oxygen species [14]. Although appropriately exposed facets of catalysts are conducive to the activation of surface lattice oxygen, high temperature is necessary to break through the limit of slow oxygen exchange rates from surface lattice oxygen to molecular O_2 in VOCs catalytic combustion [15,16].

To address this issue, increasing attention has been directed to the light-driven thermal catalytic oxidation of VOCs for taking full advantage of thermal effect of light excitation on the catalyst surface [17–20]. Compared to the conventional photocatalytic oxidation or thermal oxidation, light-driven thermal catalysis oxidation of VOCs can rapid occur on the surface of the catalyst, in which light is absorbed and then transferred to target pollutants by heat or hot electrons [21–23]. The localized high temperature of catalysts surface can drive the fast-exchange of surface lattice oxygen and gaseous oxygen, which is conducive to the rapid oxidation of VOCs and low energy loss [24,25]. However, there are no reports so far on the study about boosting light-driven surface lattice oxygen activation of catalyst materials by

^{*} Corresponding author.

E-mail address: gkzhang@whut.edu.cn (G. Zhang).

<https://doi.org/10.1016/j.apcatb.2022.122274>

Received 3 June 2022; Received in revised form 4 October 2022; Accepted 6 December 2022

Available online 9 December 2022

0926-3373/© 2022 Elsevier B.V. All rights reserved.

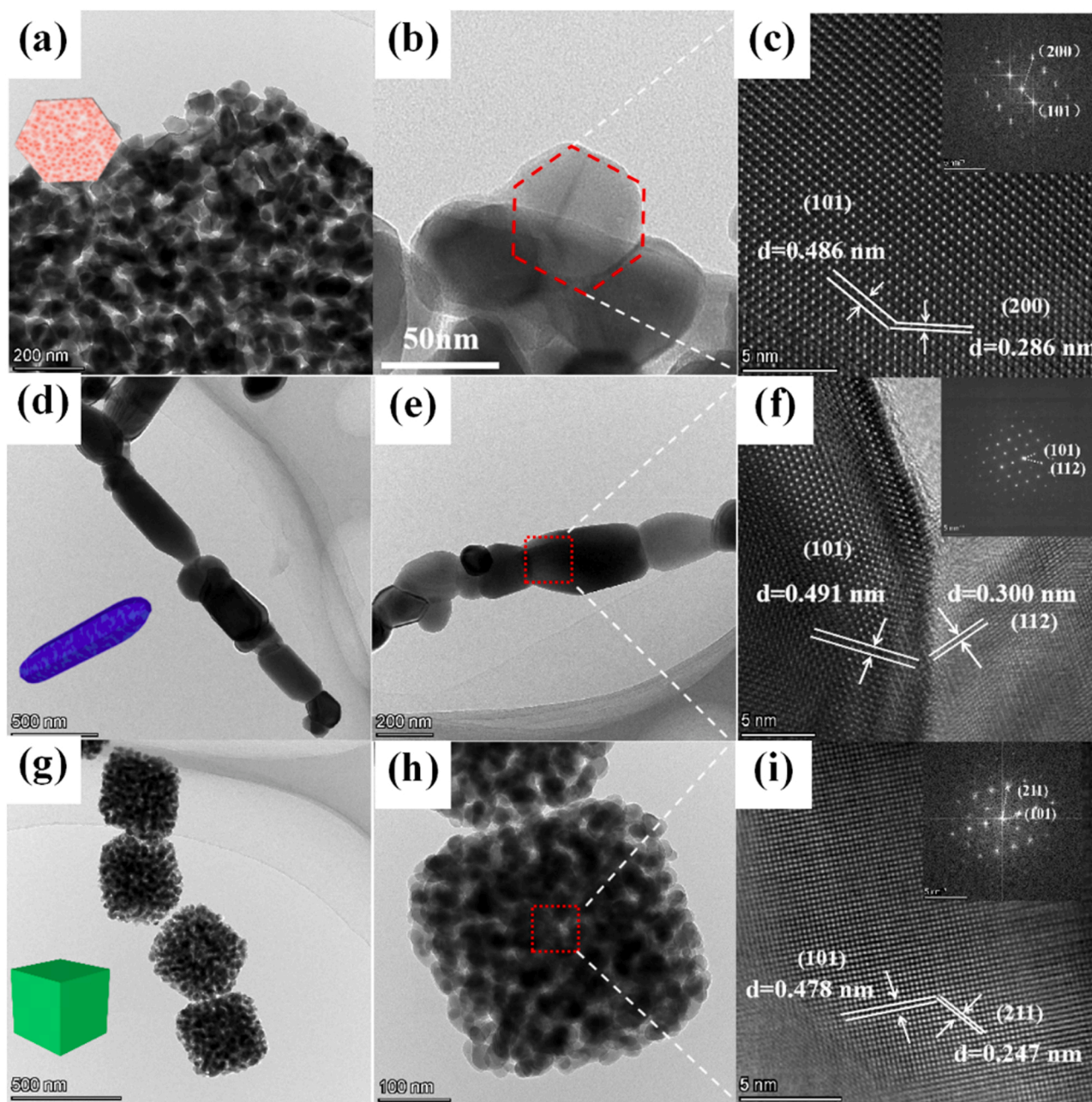


Fig. 1. TEM images of the synthesized ZnMn_2O_4 samples: ZMO-H (a-c), ZMO-R (d-f), and ZMO-C (g-i).

controllably exposed facets for photothermal mineralization of toluene.

ZnMn_2O_4 material, as one type of stable spinel oxides, can be a good platform for unveiling how to design facet-dependent ZnMn_2O_4 to active its surface lattice oxygen and promote catalytic oxidation of toluene under full-spectrum light irradiation. On one hand, it is possible to synthesize the ZnMn_2O_4 materials with different exposed facets by suitable preparation methods [26–28]. We conjecture that the surface lattice oxygen content of ZnMn_2O_4 materials with different exposed facets might be different according to the crystal growth theory [29,30]. On the other hand, the ZnMn_2O_4 material appears black, which exhibits excellent light absorption properties and photothermal conversion ability [31,32]. These excellent intrinsic properties of ZnMn_2O_4 have made the surface lattice oxygen activation of facet-dependent ZnMn_2O_4 possible at a relatively low ambient temperature. Herein, we successfully synthesized ZnMn_2O_4 with controllably exposed {010}, {11–1}, and {1–1–1} facets and firstly used them to unveil the essential role of surface lattice oxygen activation of facet-dependent ZnMn_2O_4 for

toluene photothermal mineralization under full-spectrum light irradiation. More importantly, apart from various characterization techniques, the DFT calculations were also performed to investigate the toluene photothermal reaction mechanism relating to the surface lattice oxygen activation of facet-dependent ZnMn_2O_4 . Our study showed that surface lattice oxygen activation of facet-dependent ZnMn_2O_4 plays an important role in toluene photothermal catalysis.

2. Materials and methods

2.1. Catalyst preparation

The synthesis of ZnMn_2O_4 hexagonal nanoplates with exposed {010} facets (ZMO-H) and ZnMn_2O_4 nanorods with exposed {11–1} facets (ZMO-R) were carried out via a hydrothermal method, as referred to previous literature with some modification [26,27]. As for the preparation of ZMO-H, 2 mmol $\text{Mn}(\text{CH}_3\text{COO})_2 \cdot 4\text{H}_2\text{O}$, 1 mmol Zn

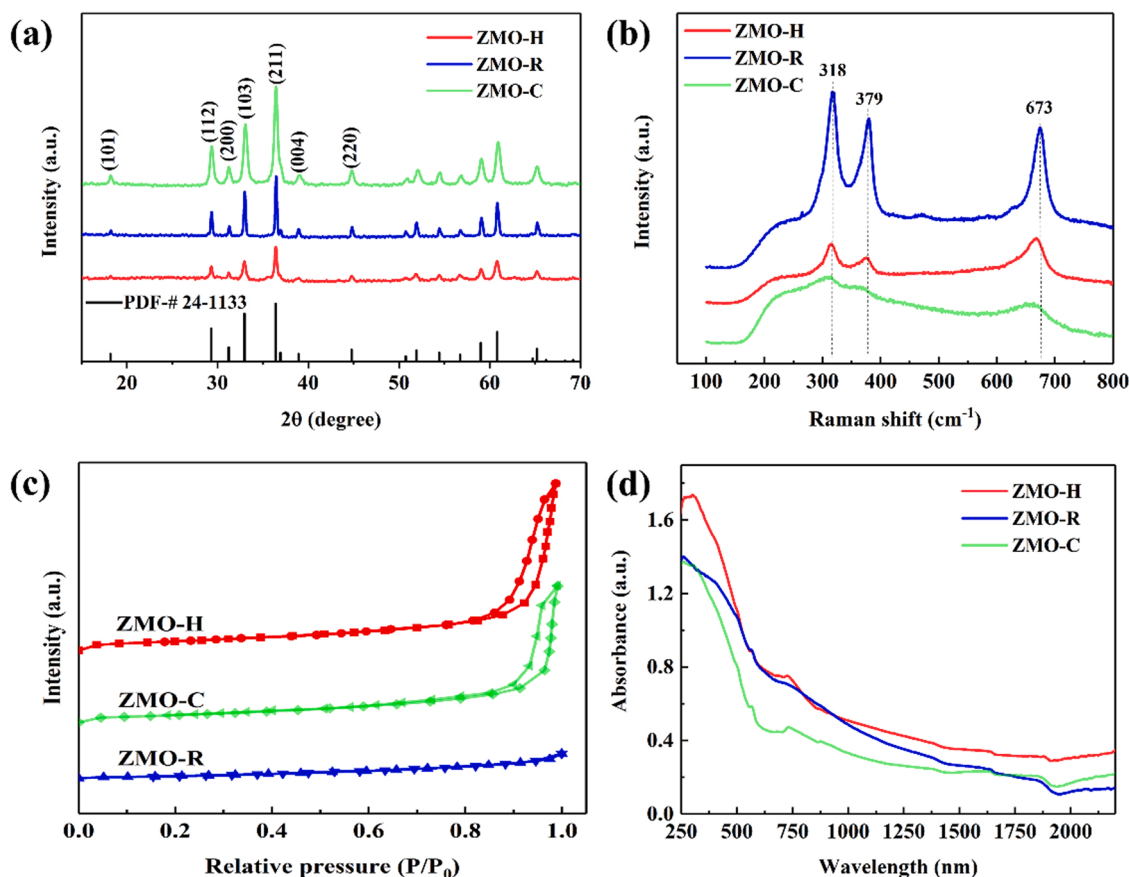


Fig. 2. XRD patterns (a), Raman spectra (b), Nitrogen adsorption and desorption isotherms (c) and UV-vis-NIR absorption spectra (d) of ZMO-H, ZMO-R and ZMO-C.

$(\text{CH}_3\text{COO})_2\cdot 2\text{H}_2\text{O}$ and 18 mmol oxalic acid were dissolved in the mixture solution of 30 mL absolute alcohol and 20 mL *N,N*-dimethylformamide (DMF). After the stirring for 3 h, the aged solution was poured into a 90 mL Teflon-lined stainless autoclave and kept at 170 °C in an oven for 8 h. The resultant precipitate was centrifuged and washed for several times, allowed to be dried overnight at 90 °C and calcined at 600 °C for 2 h under air. For the preparation of ZMO-R, Zn $(\text{CH}_3\text{COO})_2\cdot 2\text{H}_2\text{O}$ (0.297 g) and Mn $(\text{CH}_3\text{COO})_2\cdot 4\text{H}_2\text{O}$ (0.4902 g) were added into 99 mL ethanol-water (1:10 ratio v/v) mixed solution under stirring. Another solution consisting of $\text{H}_2\text{C}_2\text{O}_4\cdot 2\text{H}_2\text{O}$ (0.252 g), ethanol (45 mL) and distilled water (5 mL) was poured into the above solution quickly. After evaporating the solution for 3 h at 90 °C, the ZnMn_2O_4 precursors were collected and calcined at 450 °C and then at 700 °C for 6 h in air. The ZnMn_2O_4 nanocubes with exposed {1–1–1} facets (ZMO-C) were synthesized by a microemulsion precipitation method [28]. Typically, $\text{ZnSO}_4\cdot 7\text{H}_2\text{O}$ (0.5751 g), $\text{MnSO}_4\cdot \text{H}_2\text{O}$ (0.6761 g), and cetyltrimethylammonium bromide (3.65 g) were dissolved in the mixture solution of 10 mL distilled water, 10 mL *n*-pentanol, and 200 mL *n*-hexane. After that, 10 mL NH_4HCO_3 aqueous solution (1.2 M) was added into the above mixture solution quickly. After vigorous stirring for 5 h, the ZMO-C precursor were separated and dried in 90 °C for 10 h. Finally, the ZMO-C were obtained at 600 °C for 5 h in static air.

2.2. Catalyst characterization

The physical and chemical properties of the catalysts were characterized by XRD, SEM, TEM, BET, DRS, XPS, O_2 -TPD, CO-TPR, and in situ DRIFTS. The contents and methods of characterization are detailed described in Text S1 of the [supplementary materials](#).

2.3. DFT calculations

The role of surface lattice oxygen species in the ZnMn_2O_4 catalysts was further studied by the density functional theory (DFT) method with the Perdew-Burke-Ernzerhof (PBE) functional. The details of calculation methodology are shown in Text S2.

2.4. Catalytic activity evaluation

The light-driven catalytic activity of toluene was evaluated in a quartz window fixed bed reactor by Xenon lamp irradiation. 0.1 g of catalyst was evenly dispersed on quartz cotton with a diameter of 10 mm to prepare the catalyst layer, and a thermocouple was placed in the center of the catalyst layer to measure the surface reaction temperature. A high-precision mass flow meter was used to control the gas flow rate. The gas composition was [toluene] = 200 ppm, air = 50 vol%, and the gas hourly space velocity (GHSV) was = 36,000 $\text{mL}\cdot\text{g}^{-1}\cdot\text{h}^{-1}$. Before the light irradiation, a mixture of toluene and air was continuously penetrated for 60 min to make the catalyst adsorption saturated. The light-driven catalytic activity of toluene was tested under the Xe lamp irradiation (with 500 mW/cm^2 of light intensity). On-line quantitative analysis of reactant (toluene) and product (CO_2) was carried out by a gas chromatograph (GC9560). The toluene conversion and CO_2 yield were calculated by Eqs. (1) and (2), respectively.

$$\text{Toluene conversion} = \frac{[\text{Toluene}]_{\text{in}} - [\text{Toluene}]_{\text{out}}}{[\text{Toluene}]_{\text{in}}} \times 100\% \quad (1)$$

$$\text{CO}_2\text{ yield} = \frac{[\text{CO}_2]_{\text{produced}}}{[\text{CO}_2]_{\text{theoretical}}} \times 100\% \quad (2)$$

In the formula, the $[\text{toluene}]_{\text{in}}$ and $[\text{toluene}]_{\text{out}}$ represent the toluene

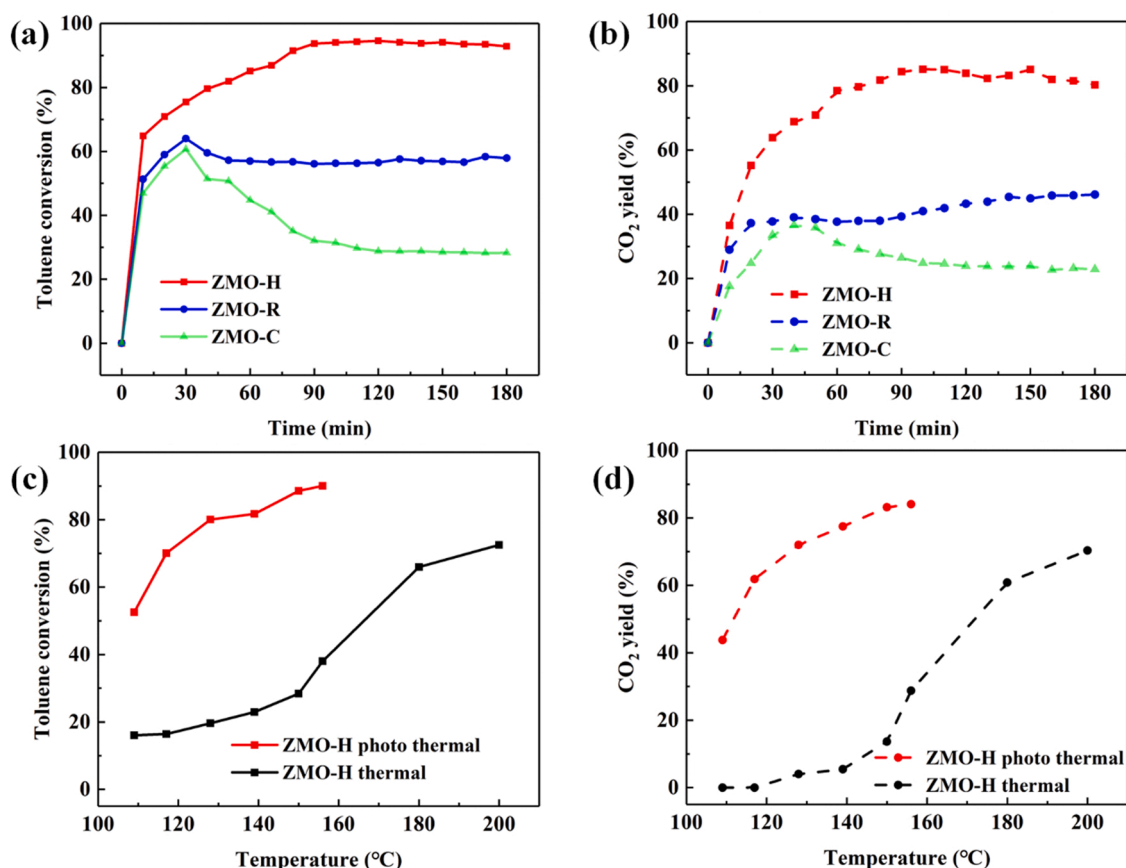


Fig. 3. Temporal evolution curves of toluene conversion (a) and CO₂ yield (b) on different samples under light intensity of 500 mW/cm², catalytic activity of ZMO-H for toluene conversion (c) and CO₂ yield (d) at different temperatures with illumination or electricity heat.

concentration at the inlet and outlet of the reactor, respectively. The $[\text{CO}_2]_{\text{produced}}$ and the $[\text{CO}_2]_{\text{theoretical}}$ respectively represent the CO₂ concentration generated by the outlet gas of the fixed-bed reactor and the theoretical value of a complete conversion from toluene to CO₂.

3. Results and discussion

3.1. Morphology and textural properties

To provide a deeper understanding of surface structure and confirm the exposed crystal facets of the synthesized ZnMn₂O₄ samples, SEM, TEM and HRTEM images were obtained and shown in Fig. S1 and Fig. 1. As shown in Fig. 1a and b, ZMO-H consists of large numbers of nano-sheets with an average width of 30 nm. The (101) and (200) crystal planes with a lattice spacing of 0.486 nm and 0.286 nm could be observed in Fig. 1c, respectively. The dominant exposed {010} facet of the ZMO-H had been identified by plane of (101) and (200), which is consistent with the results of FFT images (Fig. 1c). In addition, from statistics and calculations in Fig. S2, the percentage of dominant {010} facets of ZMO-H were 81%, which indicated that the side facets had weak influence to the dominant exposed {010} facet. Fig. 1d and e show that the ZMO-R sample consists of nanorods with an average length of 2 μm. As shown in Fig. 1f, the lattice fringe spaces of 0.491 and 0.300 nm correspond to the (101) and (112) crystal planes, respectively, which identified that the {11-1} facet is the mainly exposed facet of ZMO-R. For the ZMO-C sample, a cubic particle could be observed in Fig. 1g and h. The distinguishable lattice fringe spacing of 0.478 nm (101 plane) and 0.247 nm (211 plane) could be seen in Fig. 1i, which confirmed that the dominantly exposed facet of ZMO-C is the {1-1-1} facet. In addition, The STEM-EDX mapping in Fig. S3 showed a homogeneous distribution of Zn, Mn, O of ZMO-H, ZMO-R, and ZMO-C,

respectively.

Fig. 2 shows the structural information and properties of the prepared ZnMn₂O₄ samples, which were characterized by XRD, Raman, BET and DRS measurements. From Fig. 2a, the XRD patterns of the synthesized ZnMn₂O₄ samples with different exposed facets correspond well with the standard pattern of the spinel ZnMn₂O₄ (PDF-#24-1133, space group: I41/amd(141)). Obviously, all ZnMn₂O₄ nanocrystals exhibited similar peak positions but slightly different relative intensities of the main diffraction peaks, further confirming the preferred orientation of the ZnMn₂O₄ samples with different exposed facets. As shown in Fig. 2b, two Raman bands at the 318 cm⁻¹ and 379 cm⁻¹ for ZnMn₂O₄ different exposed facets can be attributed to the out-of-plane bending modes of Mn₂O₃ [28]. Another strong peak at 673 cm⁻¹ was attributed to the motion of oxygen inside the octahedral unit MnO₆, which confirms the formation of spinel oxides [31,32]. The structural properties of ZnMn₂O₄ samples were further characterized by FTIR spectra in Fig. S4. All three ZnMn₂O₄ samples showed strong absorption bands at 645 cm⁻¹ and 528 cm⁻¹, which also could be attributed to the spinel structure of ZnMn₂O₄ [33]. Fig. 2c showed N₂ adsorption-desorption isotherms of different ZnMn₂O₄ nanocrystals. All the three samples show type IV isotherms with a distinct H3 hysteresis loop. Surface areas, pore volumes and average pore sizes of different ZnMn₂O₄ samples were listed in Table S1 and Fig. S5. The BET surface areas of ZMO-H, ZMO-R, ZMO-C were 31.14, 9.65, and 25.01 m²/g, respectively. Similarly, the pore volumes and average pore diameter of different ZnMn₂O₄ nanocrystals were studied in Fig. S5. To unveil the role of light irradiation in surface lattice oxygen activation of ZnMn₂O₄ samples with different exposed facets, the optical absorption of ZnMn₂O₄ samples was investigated by UV-vis diffuse reflectance spectrometer (DRS) (Fig. 2d). All three ZnMn₂O₄ samples show typical intense absorption of whole solar spectrum from 250 nm to 2200 nm. The light absorption ability of

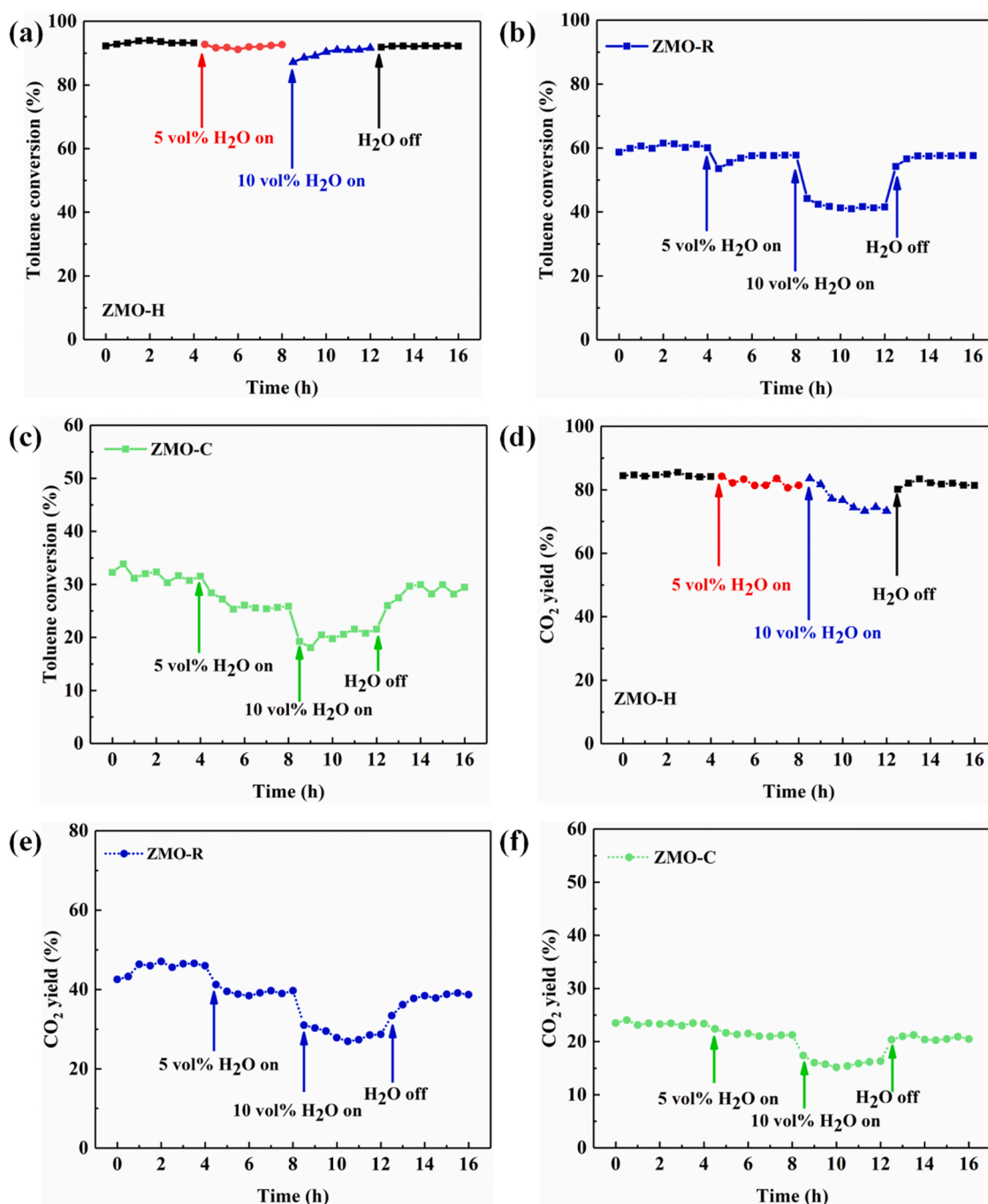


Fig. 4. Effect of H₂O on the catalytic activity of ZMO-H, ZMO-R, and ZMO-C catalysts for toluene conversion (a, b, c) and CO₂ yield (d, e, f) under Xenon lamp irradiation. (Light intensity = 500 mW/cm², WHSV = 3000 ml/(g h)).

different ZnMn₂O₄ samples could be ordered as follows: ZMO-H > ZMO-R > ZMO-C. A stronger light absorbance intensity of ZMO-H than ZMO-R and ZMO-C may induce the more effective surface lattice oxygen activation in ZMO-H [34,35].

3.2. Activity of light-driven catalytic reaction

The activities of photothermal catalytic and thermal catalytic of the synthesized ZnMn₂O₄ samples for toluene conversion and CO₂ yield were investigated in Fig. 3. As shown in Fig. 3a and b, the photothermal catalytic performances of ZnMn₂O₄ samples with different exposed facets exhibited obvious differences in toluene oxidation. At a light intensity of 500 mW/cm², the catalytic activity of ZMO-H sample reached

to maximum toluene conversion and CO₂ yield (93%, 80%) under Xenon lamp irradiation with 180 min, which were higher than that of ZMO-R sample (58%, 46%) and ZMO-C sample (28%, 23%). Although the ZMO-C have larger surface areas (in Fig. 2c) than ZMO-R, the photothermal catalytic mineralization ratio of toluene over ZMO-C was lower than that over ZMO-R, which indicated that the high BET surface areas of the catalysts was not the predominant factor to determine their photothermal catalytic performance. The catalytic performance of photothermal catalysts for toluene oxidation were also compared in Table S2. In order to compare catalytic activity under similar conditions, the initial low concentration of toluene (100–200 ppm) and WHSV (20000–32000 ml g⁻¹ h⁻¹) in recent literatures we selected is similar. It indicated that ZMO-H sample had lower catalytic temperature (158 °C)

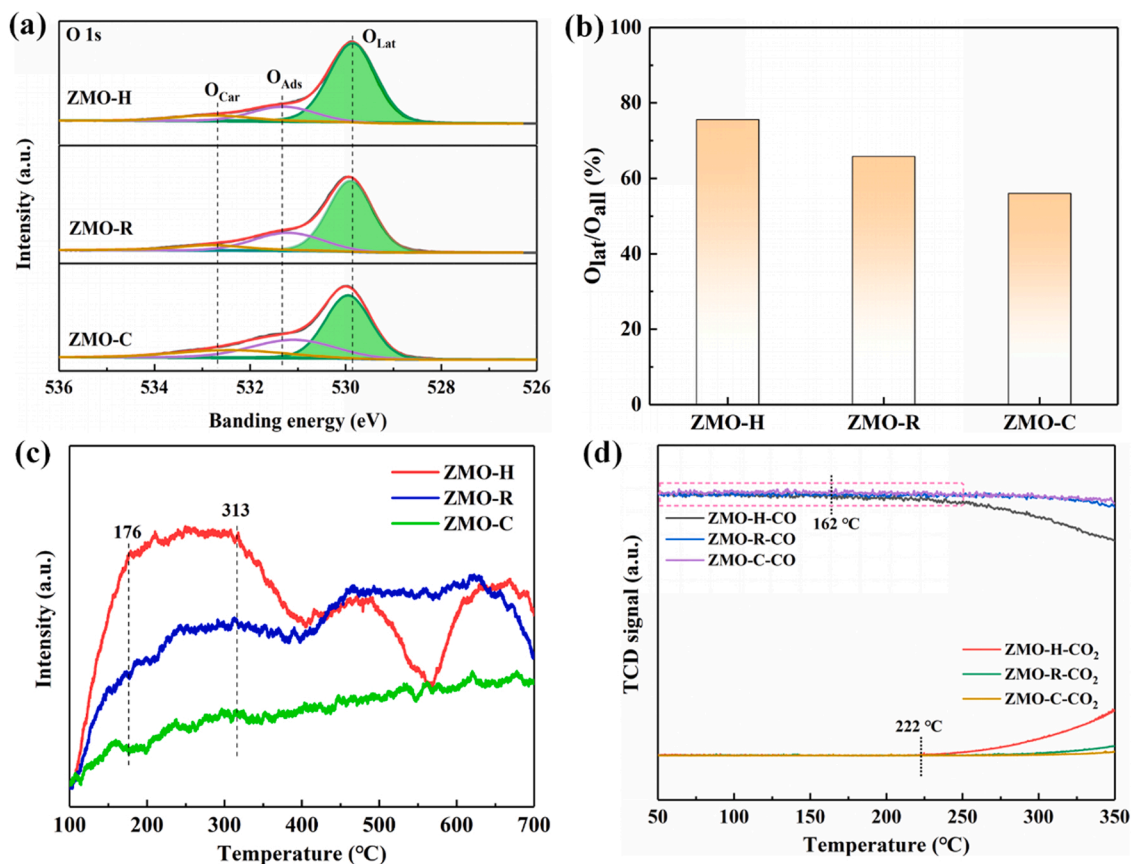


Fig. 5. O 1s XPS spectra of ZMO-H, ZMO-R, and ZMO-C (a), plotting O_{lat}/O_{all} ratio obtain from O 1s XPS spectra of ZMO-H, ZMO-R, and ZMO-C (b), O_2 -TPD profiles (c) and CO-TPR profiles (d) of ZMO-H, ZMO-R and ZMO-C.

and better catalytic activity (93% toluene conversion and 80% CO_2 yield) than most other photothermal catalysts in recent research. In addition, some studies have demonstrated that the good energy conversion ability of the catalysts from light to heat can effectively trigger the deep oxidation of VOCs [36,37]. Therefore, the system temperature of the surface layer on the catalyst had to be considered in toluene oxidation. After illuminating with the light intensity of 500 mW/cm^2 for 300 min, the final equilibrium temperatures between surface layer of ZMO-H, ZMO-R, ZMO-C and reaction vessel were around 158, 154 and 152 °C, respectively (Fig. S6). In order to study the change of temperature with irradiation time more detail, the temperature variation over time during toluene oxidation reaction was provided in Fig. S7. Under the light irradiation with the light intensity of 500 mW/cm^2 , ambient temperature of all catalysts had increased rapidly to 120 °C in 20 min. One hour after the toluene oxidation reaction, the ambient temperature for the three samples reached to relative stable and similar values. This result shows that there is little variation between the ambient temperature of different catalysts, which has limited influence for the toluene catalytic oxidation. To elucidate the excellent catalytic activity of ZMO-H under illumination, the oxidation reaction of toluene over the catalyst was investigated under light irradiation and electric heating at the same temperature. It became evident that toluene conversion and CO_2 yield (92% and 82% under 158 °C) under irradiation over ZMO-H was higher than that (41% and 30%) under electric heating at the same reaction temperature (Fig. 3c and d). Conversely, the ZMO-R (Fig. S8) and ZMO-C (Fig. S9) samples both exhibited low catalytic activity for toluene oxidation no matter under light driven or electrothermal actuation, which may be related to the difficult activation of surface lattice oxygen over ZMO-R and ZMO-C.

3.3. Photothermal catalytic stability of $ZnMn_2O_4$ with different exposed facets

The long-term stability is an important parameter for practical application of catalysts. Hence, we carried out the continuously test for the toluene oxidation over ZMO-H, ZMO-R, and ZMO-C catalysts under the Xenon lamp irradiation (Light intensity = 500 mW/cm^2). As shown in Fig. 4a, the toluene conversion of the ZMO-H catalyst was not reduced with the introduction of 5 vol% H_2O into the reaction stream. After introducing 10 vol% H_2O , toluene conversion was slightly decreased, due to the water vapor inhibits the adsorption and activation of toluene on the catalyst surface [38]. In addition, the toluene conversion could be recovered to the original values after turning off H_2O , indicating that this deactivation is reversible on the ZMO-H catalyst. The XRD patterns of the ZMO-H in Fig. S10 revealed that its structure did not change before and after photothermal reaction. The thermogravimetric analysis results of ZMO-H, ZMO-R, and ZMO-C also indicated that all three samples display a high structural stability, even at high temperatures of 800 °C (Fig. S11). In addition, after introducing 5 vol% and 10 vol% H_2O , the toluene conversions of the ZMO-R (Fig. 4b) and ZMO-C (Fig. 4c) catalysts obviously declined. The toluene conversion could not be recovered after turning off water vapor, demonstrating that the catalysts of ZMO-R and ZMO-C had poor catalytic stability. In order to explore the effect of water on the degradation of toluene, the in situ DRIFTS spectra of toluene on different catalysts were analyzed in Fig. S12. In situ DRIFTS analysis on ZMO-H under exposure to toluene (Fig. S12a) indicated that the intensity of characteristic absorption peaks at 1401 and 1526 cm^{-1} (belongs to the COO- asymmetry and symmetry vibrations of benzoate) did not significant change in the absence of H_2O or not. However, after introducing 10 vol% H_2O , the intensity of benzoate characteristic peaks was obviously reduced in Fig. S12b and

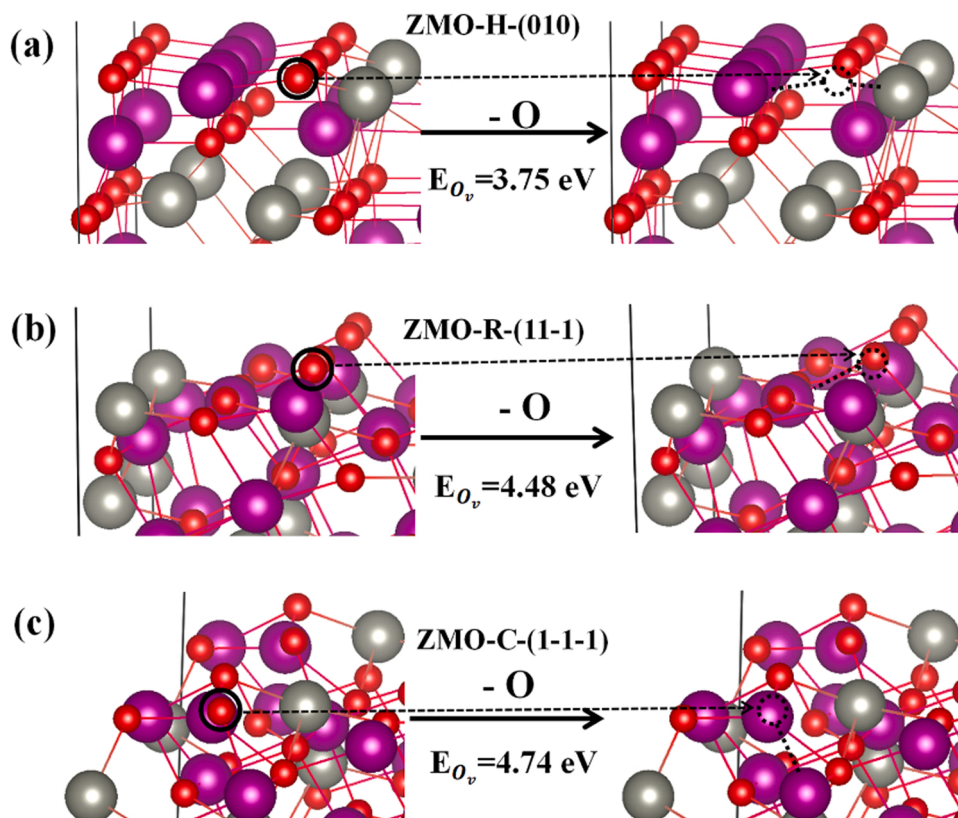


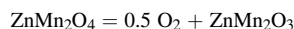
Fig. 6. The oxygen dissociation energy (E_{Ov}) required to remove one oxygen atom of ZMO-H (a), ZMO-R (b), and ZMO-C (c) supercell.

Fig. S12c. The above results indicated that the formation of benzoate on ZMO-R and ZMO-C is obviously affected after introducing the water, which did permanent damage for toluene oxidation on ZMO-R and ZMO-C. This result was further confirmed by a long-term stability test of the ZMO-H, ZMO-R, and ZMO-C for CO₂ yield, respectively (Fig. 4d-f). The CO₂ yield of the ZMO-H sample could be slightly effected when introduction of 10 vol% H₂O, and it could recover to the original value after cutting off H₂O (Fig. 4d). However, the water vapor was also permanent deleterious effect on CO₂ yield of the ZMO-R (Fig. 4e) and ZMO-C samples (Fig. 4f).

3.4. Photothermal catalytic mechanism for toluene oxidation

To probe the role of surface lattice oxygen of ZnMn₂O₄ with different exposed facets, the surface chemical composition of ZnMn₂O₄ samples were investigated by XPS technique. All the XPS spectra of O 1s could be fitted into three peaks centered at ca. 529.8, 531.2, and 532.7 eV, which could be attributed to surface lattice oxygen (O_{Lat}), surface adsorbed species (O_{Ads}), and carbonates (O_{Car}), respectively [39,40] (Fig. 5a). Fig. 5b and Table S3 presented the results of oxygen species percentage of different samples. It should be observed that the ratio of O_{Lat}/O_{All} of ZMO-H, ZMO-R, and ZMO-C were 75.6%, 65.8%, and 56%, respectively, which was consistent with the order of their catalytic activity. This results demonstrated that surface lattice oxygen might play an essential role in the photothermal catalytic of toluene according to the MvK mechanism. The peaks at 653.5 and 641.7 eV in Fig. S13a were ascribed to Mn 2p_{1/2} and Mn 2p_{3/2}, respectively [41]. In Fig. S13b, the two peaks exhibited at 1021.6 and 1044.5 eV attributed to Zn 2p_{1/2} and Zn 2p_{3/2} [42]. As shown in Fig. 5c, O₂-TPD analysis was used to further assess the ability of surface lattice oxygen releasing of different samples and understand the reasons for the high catalytic performance of the ZMO-H catalyst. Obviously, the intensity of the oxygen desorption peak of the ZMO-H sample at around 176–313 °C was much stronger than that of

ZMO-R, and ZMO-C samples. This may be due to metal-O bonds of ZMO-H were weakened and became easily broken after light driven, which was in close agreement with the results of O1s XPS analysis in Fig. 5a. As shown in Fig. 5d, the CO consumption curve and CO₂ generation curve indicated that the ZMO-H sample with argon pretreatment starts to consume CO and generate CO₂ at 162 °C and 222 °C, respectively, which is due to the consumption of surface lattice oxygen at the surface of ZMO-H [43–45]. Compared with that of ZMO-R and ZMO-C, it is clear that more surface lattice oxygen was consumed on the ZMO-H surface at the low temperature region (50–350 °C). The enlarged graph (Fig. S14) of CO-TPR profiles also confirmed that the surface lattice oxygen of ZMO-H is more easily activated than ZMO-R and ZMO-C. To further investigations of the specific role played by the surface lattice oxygen, we carried out a theoretical study to calculate the oxygen dissociation energy (E_{Ov}) of removing one oxygen atom from ZnMn₂O₄ supercell using DFT:



$$E_{Ov} = E_{\text{def}} + 0.5E_{\text{O}_2} - E_{\text{bulk}}$$

Where E_{def} represents the energy of the ZnMn₂O₃ supercell, E_{bulk} represents the energy of the ZnMn₂O₄ supercell, and E_{O_2} represents the energy of O₂ in gas phase.

The original data for the calculation of the oxygen dissociation energy (E_{Ov}) required to remove one oxygen atom of ZnMn₂O₄ supercell were summarized in Table S4. For the ZnMn₂O₄ (010) which simulated ZMO-H surface, the E_{Ov} of removing one oxygen atom from the ZMO-H supercell is 3.75 eV (Fig. 6a), which was lower than that of ZMO-R (4.48 eV), and ZMO-C (4.74 eV) supercell in Fig. 6b and c. This DFT calculation revealed that the surface lattice oxygen of ZMO-H was easily activated than that of ZMO-R and ZMO-C, which was consistent with the results of O₂-TPD and CO-TPR in Fig. 5c and Fig. 5d, respectively.

DFT calculations were also conducted to explore the adsorption of

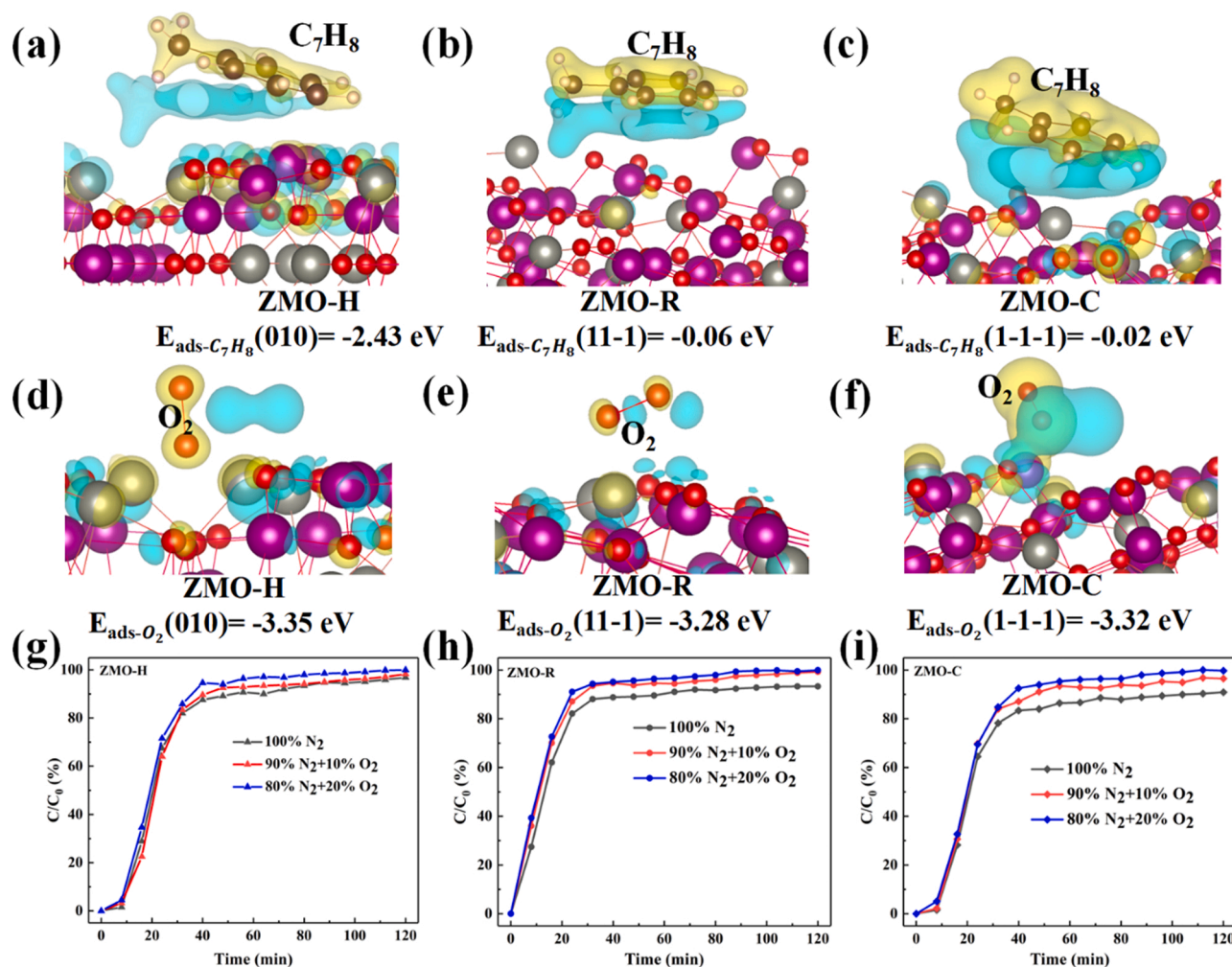


Fig. 7. Adsorption of toluene molecules over the ZMO-H surface (a), ZMO-R surface (b), and ZMO-C surface (c); Adsorption of oxygen molecules over the ZMO-H surface (d), ZMO-R surface (e), and ZMO-C surface (f), adsorption breakthrough curves of toluene on ZMO-H (g), ZMO-R (h), and ZMO-C (i) under different O_2 concentrations (Initial concentration of toluene: 200 ppm, gas flow: 50 ml/min).

toluene and gaseous oxygen on the ZnMn₂O₄ samples. The calculated adsorption energy of toluene molecules ($E_{\text{ads-toluene}}$) over ZMO-H, ZMO-R, and ZMO-C surface were shown in Fig. 7a-c and Table S5. Fig. 7a-c showed that the $E_{\text{ads-toluene}}$ over the ZnMn₂O₄ with exposed {010}, {11-1}, and {1-1-1} facets were -2.43 , -0.06 and -0.02 eV , respectively. Due to the more negative adsorption energy of ZMO-H with {010} exposed facets, the toluene molecules were preferentially adsorbed on the surface of ZMO-H, which may promote the toluene molecules more readily to be activated and deep oxidized. The adsorption energies of gaseous oxygen ($E_{\text{ads-}O_2}$) over ZMO-H, ZMO-R, and ZMO-C are -3.35 , -3.28 , and -3.32 eV , which were shown in Fig. 7d-f and Table S6. The similar adsorption energy of the three samples for O_2 is beneficial for us to study the role of activation of surface lattice oxygen by oxygen dissociation energy (E_{O_2}) after eliminating the influence of $E_{\text{ads-}O_2}$. In addition, the co-adsorption process of toluene and O_2 on the different catalysts (ZMO-H, ZMO-R, and ZMO-C) was also discussed in Fig. 7g-i. As shown in Fig. 7g, the adsorption capacity of toluene over ZMO-H displayed subtle distinction at the different O_2 concentration streams (20%, 10%, and 0% O_2), which were opposite to the results over ZMO-R (Fig. 7h) and ZMO-C (Fig. 7i). When the O_2 adsorbed on the surface of ZMO-R and ZMO-C, O_2 could occupy the adsorption site easily due to the greater adsorption energy difference between toluene and O_2 on ZMO-R (3.22 eV) and ZMO-C (3.30 eV) than that on ZMO-H (0.92 eV), which indicated that the competitive adsorption between the two molecules is more likely to occur on the surface of ZMO-R and ZMO-C

than that on ZMO-H [46,47].

In order to understand the role of surface lattice oxygen in ZnMn₂O₄ on the photothermal catalytic degradation of toluene, in situ DRIFTS analysis method was applied to study the reaction pathway over ZnMn₂O₄ samples with different exposed facets (Fig. 8). Fig. 8a showed the DRIFTS spectra of ZMO-H as a function of time in the absence of oxygen containing 2000 ppm toluene. First, toluene was adsorbed on ZMO-H in N_2 for 30 min until the DRIFT spectral remained unchanged. From the spectrum at 30 min, the bands at 3027 and 2926 cm^{-1} were assigned to the C-H stretching vibration of the methyl ($-CH_3$) group [48, 49]. The bands at 1379, 1460, 1495, and 1605 cm^{-1} could be ascribed to the stretching vibration of aromatic ring [49-51]. After toluene was adsorbed to a saturation state with 30 min, the temperature of the reaction chamber was gradually heated to 160 $^{\circ}\text{C}$ with auxiliary light irradiation. It was observed some bands of toluene decrease rapidly, while some new characteristic peaks appeared, demonstrating that some reactions take place on the surface of ZMO-H. A peak at 1146 and 1255 cm^{-1} belongs to C-O vibration of the benzyloxy group [51,52]. The bands at 2837 cm^{-1} corresponded to a C-H stretching vibration of the $-CH_2O-$ in the benzyloxy group [53,54]. The peaks at 1398 and 1520 cm^{-1} were attributed to COO- asymmetry and symmetry vibrations of benzoate, which indicated that benzoate species could be formed in the absence of gas-phase oxygen [55]. As no external oxygen was introduced into the reaction chamber, carboxylates were still formed on the surface of ZMO-H, which illustrated that the reactive

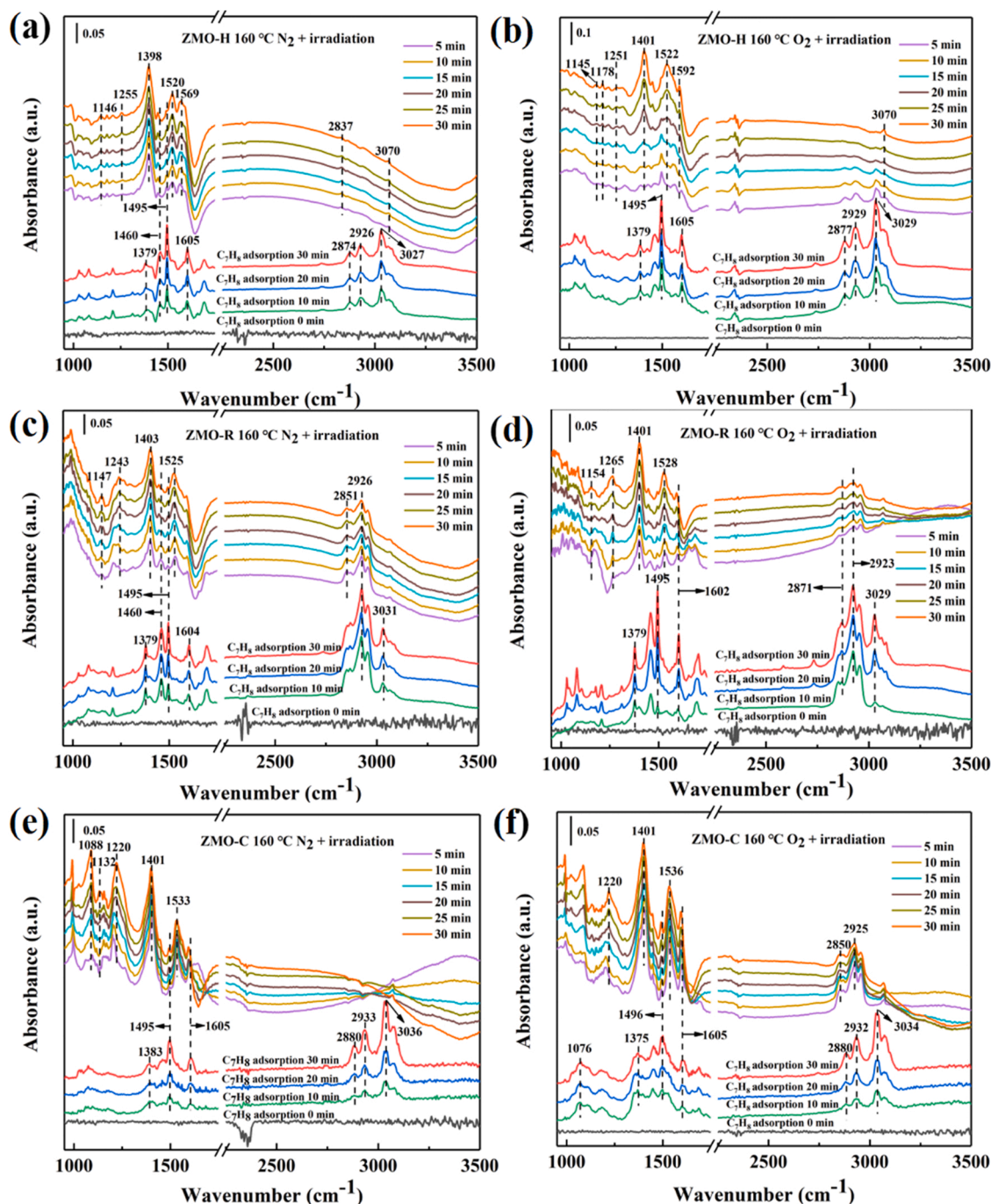


Fig. 8. In situ DRIFTS analysis on ZMO-H catalyst under exposure to toluene in air (a) and N_2 (b) at 160 °C with light irradiation; In situ DRIFTS analysis on ZMO-R catalyst under exposure to toluene in air (c) and N_2 (d) at 160 °C with light irradiation; In situ DRIFTS analysis on ZMO-C catalyst under exposure to toluene in air (e) and N_2 (f) at 160 °C with light irradiation.

oxygen species originated from the interior of ZMO-H. That is, the surface lattice oxygen may play an important role in this catalytic process. Due to insufficient external oxygen provision, the aromatic ring of toluene did not disappear at high temperatures, which was in accordance with the persistence of stretching vibration of aromatic ring at 1460 and 1495 cm^{-1} . As shown in Fig. 8b, under identical conditions, the introduction of gaseous oxygen could effectively accelerate the generation of toluene intermediate products during the photothermal catalytic reaction. Except that the peaks of aromatic rings gradually disappeared at 1460 and 1495 cm^{-1} , the characteristic peaks intensity of benzaldehyde and benzoic acid were stronger than that under N_2 . Besides, the characteristic peaks of maleic anhydride at 1251 and

1592 cm^{-1} could also be observed at 160 °C with light irradiation. The intermediate products were mainly attributed to benzaldehyde, benzoic acid and maleic anhydride.

Similar experimental procedures were also carried out over ZMO-R and ZMO-C. Fig. 8c show the time-resolved in situ DRIFTS spectra of ZMO-R under exposure to toluene in N_2 . Similar toluene adsorption and chemical conversion process could be observed on the surface of ZMO-R. As shown in Fig. 8d, the characteristic peaks of benzyloxy species (1154 cm^{-1}), benzaldehyde species (1265 cm^{-1}) over ZMO-R were more intensive compared to those over ZMO-H (Fig. 8b), while less intensity bands of benzoate species (1401, 1528 cm^{-1}) were found over ZMO-R than ZMO-H. Especially, the aromatic ring signal of toluene

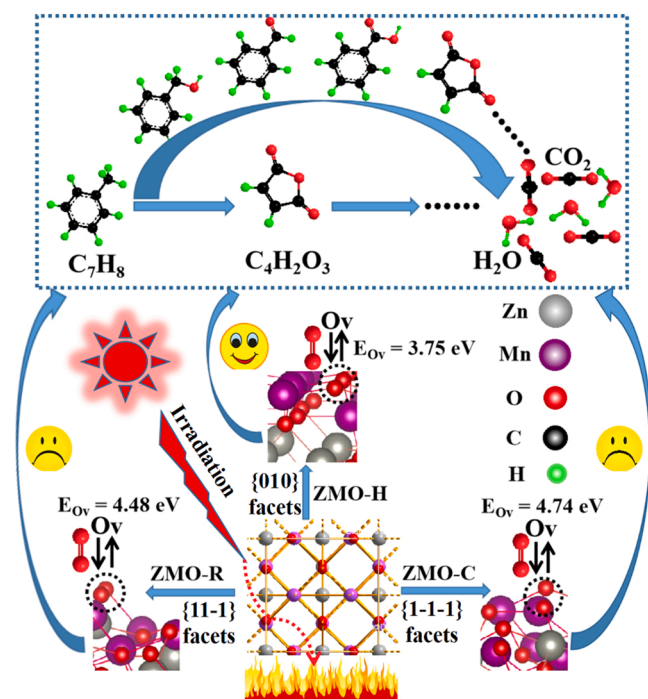


Fig. 9. Schematic of the potential mechanisms for the photothermal catalytic of toluene over spinel ZnMn₂O₄ with different exposed facets.

(1602 cm⁻¹) over ZMO-R did not disappear in air at 160 °C with light irradiation. In addition, the C=O stretching vibration of maleic anhydride species did not appear at 1251 and 1592 cm⁻¹.

Fig. 8e and f show the in situ DRIFTS analysis on ZMO-C catalyst under exposure to toluene in air and N₂ at 160 °C with light irradiation. We found that characteristic peaks of toluene aromatic ring at 1460, 1495, and 1605 cm⁻¹ did not completely disappear either in the absence of gas oxygen (Fig. 8e) or not (Fig. 8f and Fig. S15a). The local magnification graph (Fig. S15b) of Fig. 8d also showed that the skeletal vibrations peaks of aromatic ring on ZMO-R still exist after reaction for 30 min at 160 °C with light irradiation. However, the skeletal vibrations peaks of aromatic ring on ZMO-H had disappeared quickly after toluene oxidation reaction for 15 min (Fig. S15c). This results reveal that the ring-opening process is the rate-determining step for photothermal oxidation of toluene [56,57]. The bands of all benzoate species (1401, 1536 cm⁻¹) over ZMO-C in Fig. 8f were far less intensive compared to those over ZMO-H (Fig. 8b) and ZMO-R (Fig. 8d). Besides, no bands ascribed to maleic anhydride species could be observed over ZMO-C. Comparing the adsorption species on ZnMn₂O₄ with different exposed facets in Fig. 8b, d, and f, the amounts of benzoate species followed the order: ZMO-H > ZMO-R > ZMO-C, in accordance with their photothermal catalytic performance of toluene mineralization. These results indicated that a stronger surface lattice oxygen activation of ZMO-H may lead to the deeper oxidation of toluene than that to ZMO-R and ZMO-C, which was consistent with the results of XPS, O₂-TPD, CO-TPR analysis and DFT calculations.

From the results in this study, a possible mechanism (Fig. 9) for the photothermal catalytic mineralization of toluene over spinel ZnMn₂O₄ with different exposed facets was proposed. The reaction path primarily follows the Mars-van Krevelen mechanism, in which surface lattice oxygen plays a decision role: toluene was initially adsorbed on the surface of ZnMn₂O₄, -CH₃ of adsorbed toluene was attacked by surface lattice oxygen to generate benzyl species under light-driven. The benzyl species could be further oxidized to carboxylate and anhydride species in consecutive. Finally, this intermediates were fully oxidized to CO₂ and H₂O after the sustainable replenishment of gaseous oxygen. The different intermediates among ZMO-H, ZMO-R, and ZMO-C confirmed a

new ring-opening pathway in which the aromatic ring of toluene could directly open from maleic anhydride over ZMO-H due to its lower oxygen dissociation energy. In this process, chemisorbed oxygen molecules were inclined to replenish the oxygen vacancy and activation of the surface lattice oxygen by light irradiation, which promoted the circulation of photothermal catalytic oxidation of toluene. Therefore, the surface lattice oxygen plays a decision role for the enhanced photothermal mineralization efficiency of toluene over ZnMn₂O₄ catalyst with appropriate exposed facets.

4. Conclusion

In this work, we have expanded a crystal engineering strategy for preparation of controllably facets exposed ZnMn₂O₄ and photothermal oxidation of toluene. Due to its stronger ability of surface lattice oxygen activation, the better toluene adsorption performance, the ZMO-H catalyst with exposed {010} facet exhibits best photothermal catalytic performance (the toluene conversion and CO₂ yield are 93% and 80%, respectively). Additionally, it can also keep toluene conversion above 92% after the 480 min stability test in the presence of water vapor (5 vol %). The in situ DRIFTS spectra revealed the reaction route for toluene oxidation on ZMO-H may follow the benzylalcohol-benzaldehyde-benzoate-maleic anhydride pathway. Our research provides a novel insight from the design of nanostructured materials with enhancing activation ability of surface lattice oxygen to understanding the photothermal mechanism of toluene removal by light-driven.

CRediT authorship contribution statement

Qiang Cheng: Experiment, Data processing & analysis, Writing – original draft, Revised manuscript preparation. **Yuan Li:** Data analysis, Writing – review & editing. **Zhuangzhuang Wang:** Data analysis, Writing – review & editing. **Xiaotian Wang:** Data analysis, Writing – review & editing. **Gaoke Zhang:** Design the idea, Writing – review & editing, Resources.

Declaration of Competing Interest

The authors declare that they have no known competing financial interests or personal relationships that could have appeared to influence the work reported in this paper.

Data Availability

Data will be made available on request.

Acknowledgments

The study was supported by the National Natural Science Foundation of China (NSFC No. 92163125) and Science and Technology Planning Project of Shenzhen Municipality (JCYJ20200109150225155).

Appendix A. Supporting information

Supplementary data associated with this article can be found in the online version at doi:10.1016/j.apcatb.2022.122274.

References

- [1] A. Grimaud, O. Diaz-Morales, B. Han, W.T. Hong, Y.-L. Lee, L. Giordano, K. A. Stoerzinger, M.T.M. Koper, Y. Shao-Horn, Activating lattice oxygen redox reactions in metal oxides to catalyse oxygen evolution, *Nat. Chem.* 9 (2017) 457–465, <https://doi.org/10.1038/NCHEM.2695>.
- [2] Z. Wu, T. Liao, S. Wang, J.A. Mudiyansele, A.S. Micallef, W. Li, J. Yang, W. Luo, K. Ostrikov, Y. Gu, Z. Sun, 2022. Conversion of catalytically inert 2D bismuth oxide nanosheets for effective electrochemical hydrogen evolution reaction catalysis via oxygen vacancy concentration modulation, *Nano-Micro Lett.* 2022, DOI:10.1007/s40820-022-00832-6, <https://doi.org/10.1007/s40820-022-00832-6>.

- [3] Y. Li, Z. Hua, Y. Wu, Y. Zeng, Z. Qiu, X. Tian, M. Wang, E. Li, Modified impregnation synthesis of Ru-loaded WO_3 nanoparticles for acetone sensing, *Sens. Actuators B-Chem.* 265 (2018) 249–256, <https://doi.org/10.1016/j.snb.2018.03.037>.
- [4] X. Wang, Z. Wang, Y. Li, J. Wang, G. Zhang, Efficient photocatalytic CO_2 conversion over 2D/2D Ni-doped $\text{CsPbBr}_3/\text{Bi}_2\text{O}_3$ Z-scheme heterojunction: critical role of Ni doping, boosted charge separation and mechanism study, *Appl. Catal. B-Environ.* 319 (2022), 121895 <https://doi.org/10.1016/j.apcatb.2022.121895>.
- [5] I. Heo, S. Sung, M.B. Park, T.S. Chang, Y.J. Kim, B.K. Cho, S.B. Hong, J.W. Choung, I.-S. Nam, Effect of hydrocarbon on DeNO_x performance of selective catalytic reduction by a combined reductant over Cu-containing zeolite catalysts, *ACS Catal.* 9 (2019) 9800–9812, <https://doi.org/10.1021/acscatal.9b02763>.
- [6] P. Liu, Y. Liao, J. Li, L. Chen, M. Fu, P. Wu, R. Zhu, X. Liang, T. Wu, D. Ye, Insight into the effect of manganese substitution on mesoporous hollow spinel cobalt oxides for catalytic oxidation of toluene, *J. Colloid Interf. Sci.* 594 (2021) 713–726, <https://doi.org/10.1016/j.jcis.2021.03.093>.
- [7] R. Cao, L. Li, P. Zhang, L. Gao, S. Rong, Regulating oxygen vacancies in ultrathin I-MnO_2 nanosheets with superior activity for gaseous ozone decomposition, *Environ. Sci.: Nano* 8 (2021) 1628, <https://doi.org/10.1039/d1en00149c>.
- [8] J. Chen, H. Tang, M. Huang, Y. Yan, J. Zhang, H. Liu, J. Zhang, G. Wang, R. Wang, Surface lattice oxygen activation by nitrogen-doped manganese dioxide as an effective and longevous catalyst for indoor HCHO decomposition, *ACS Appl. Mater. Interfaces* 13 (2021) 26960–26970, <https://doi.org/10.1021/acscami.1c04369>.
- [9] S. Das, A. Jangam, S. Jayaprakash, S. Xi, K. Hidajat, K. Tomishige, S. Kawi, Role of lattice oxygen in methane activation on Ni-phylosilicate/ $\text{Ce}_{1-x}\text{Zr}_x\text{O}_2$ core-shell catalyst for methane dry reforming: Zr doping effect, mechanism, and kinetic study, *Appl. Catal. B-Environ.* 290 (2021), 119998 <https://doi.org/10.1016/j.apcatb.2021.119998>.
- [10] Y. Zhong, C. Peng, Z. He, D. Chen, H. Jia, J. Zhang, H. Ding, X. Wu, Interface engineering of heterojunction photocatalysts based on 1D nanomaterials, *Catal. Sci. Technol.* 11 (2021) 27, <https://doi.org/10.1039/d0cy01847c>.
- [11] W. Zhu, X. Chen, C. Li, Z. Liu, C. Liang, Manipulating morphology and surface engineering of spinel cobalt oxides to attain high catalytic performance for propane oxidation, *J. Catal.* 396 (2021) 179–191, <https://doi.org/10.1016/j.jcat.2021.02.014>.
- [12] G. Zhai, J. Wang, Z. Chen, W. An, Y. Men, Boosting soot combustion efficiency of Co_3O_4 nanocrystals via tailoring crystal facets, *Chem. Eng. J.* 337 (2018) 488–498, <https://doi.org/10.1016/j.cej.2017.12.141>.
- [13] Y. Wei, Y. Zhang, P. Zhang, J. Xiong, X. Mei, Q. Yu, Z. Zhao, J. Liu, Boosting the removal of diesel soot particles by the optimal exposed crystal facet of CeO_2 in Au/ CeO_2 catalysts, *Environ. Sci. Technol.* 54 (2020) 2002–2011, <https://doi.org/10.1021/acs.est.9b07013>.
- [14] X. Zhu, B. Bai, B. Zhou, S. Ji, Co_3O_4 nanoparticles with different morphologies for catalytic removal of ethyl acetate, *Catal. Commun.* 156 (2021), 106320, <https://doi.org/10.1016/j.catcom.2021.106320>.
- [15] Z. Hu, X. Liu, D. Meng, Y. Guo, Y. Guo, G. Lu, Effect of ceria crystal plane on the physicochemical and catalytic properties of Pd/Ceria for CO and propane oxidation, *ACS Catal.* 6 (2016) 2265–2279, <https://doi.org/10.1021/acscatal.5b02617>.
- [16] J. Niu, H. Liu, Y. Zhang, X. Wang, J. Han, Z. Yue, E. Duan, NiCo_2O_4 spinel for efficient toluene oxidation: the effect of crystal plane and solvent, *Chemosphere* 259 (2020), 127427, <https://doi.org/10.1016/j.chemosphere.2020.127427>.
- [17] M. Li, Y. Wang, Y. Fan, L. Liao, X. Zhou, S. Mo, H. Wang, Controllable synthesis various morphologies of 3D hierarchical $\text{MnO}_x\text{-TiO}_2$ nanocatalysts for photothermocatalysis toluene and NO with free-ammonia, *J. Colloid Interf. Sci.* 608 (2022) 3004–3012, <https://doi.org/10.1016/j.jcis.2021.11.029>.
- [18] Z. Wang, S. Xie, Y. Feng, P. Ma, K. Zheng, E. Duan, Y. Liu, H. Da, J. Deng, Simulated solar light driven photothermal catalytic purification of toluene over iron oxide supported single atom Pt catalyst, *Appl. Catal. B-Environ.* 298 (2021), 120612, <https://doi.org/10.1016/j.apcatb.2021.120612>.
- [19] M. Zhang, H. Gao, J. Chen, E.A. Elimian, H. Jia, Calcination engineering of urchin-like $\text{CoO}_x\text{-CN}$ catalysts to enhance photothermocatalytic oxidation of toluene via photo-/thermo-coupling effect, *Appl. Catal. B-Environ.* 307 (2022), 121208, <https://doi.org/10.1016/j.apcatb.2022.121208>.
- [20] Y. Guo, M. Wen, S. Song, Q. Liu, G. Li, T. An, Enhanced catalytic elimination of typical VOCs over ZnCoO_x catalyst derived from in situ pyrolysis of ZnCo bimetallic zeolitic imidazolate frameworks, *Appl. Catal. B-Environ.* 308 (2022), 121212, <https://doi.org/10.1016/j.apcatb.2022.121212>.
- [21] Y.-J. Hao, Y.-G. Ma, X. Zhang, J. Li, S. Wang, X. Chen, F.-T. Li, Unraveling the importance between electronic intensity and oxygen vacancy on photothermocatalytic toluene oxidation over CeO_2 , *Chem. Eng. J.* 433 (2022), 134619, <https://doi.org/10.1016/j.cej.2022.134619>.
- [22] X. Chen, G. Zhang, B. Li, L. Wu, An integrated giant polyoxometalate complex for photothermally enhanced catalytic oxidation, *Sci. Adv.* 7 (2021) 8413 (<http://advances.sciencemag.org>).
- [23] Y. Zeng, J. Zhong, H. Wang, M. Fu, D. Ye, Y. Hu, Synergistic effect of tunable oxygen-vacancy defects and graphene on accelerating the photothermal degradation of methanol over $\text{Co}_3\text{O}_4/\text{rGO}$ nanocomposites, *Chem. Eng. J.* 425 (2021), 131658, <https://doi.org/10.1016/j.cej.2021.131658>.
- [24] Y. Yang, S. Wu, Y. Li, Q. Zhang, X. Zhao, Efficient UV–vis-IR photothermocatalytic selective ethanol oxidation on $\text{MnO}_x/\text{TiO}_2$ nanocomposites significantly enhanced by a novel photoactivation, *J. Mater. Chem. A* 8 (2020) 1254, <https://doi.org/10.1039/c9ta12531k>.
- [25] J. Kong, C. Jiang, Z. Rui, S. Liu, F. Xian, W. Ji, H. Ji, Photothermocatalytic synergistic oxidation: An effective way to overcome the negative water effect on supported noble metal catalysts for VOCs oxidation, *Chem. Eng. J.* 397 (2020), 125485, <https://doi.org/10.1016/j.cej.2020.125485>.
- [26] H. Cao, X. Xiao, X. Wang, J. Liu, P. Si, Morphology engineering of self-assembled porous zinc manganite hexagons for lithium ion storage, *Electrochim. Acta* 330 (2020), 135260, <https://doi.org/10.1016/j.electacta.2019.135260>.
- [27] Y. Tian, Z. Chen, W. Tang, Z. Yang, W. Zhang, S. Li, K. Wang, Y. Sun, Q. Xia, B. Guo, A facile synthetic protocol to construct 1D Zn-Mn-Oxide nanostructures with tunable compositions for high-performance lithium storage, *J. Alloy. Compd.* 720 (2017) 376–382, <https://doi.org/10.1016/j.jallcom.2017.05.218>.
- [28] S. Chen, M. Yao, F. Wang, J. Wang, Y. Zhang, Y. Wang, Facile microemulsion synthesis of mesoporous ZnMn_2O_4 submicrocubes as high-rate and long-life anodes for lithium ion batteries, *Ceram. Int.* 45 (2019) 5594–5600, <https://doi.org/10.1016/j.ceramint.2018.12.019>.
- [29] R. Mi, D. Li, Z. Hu, R.T. Yang, Morphology effects of CeO_2 nanomaterials on the catalytic combustion of toluene: a combined kinetics and diffuse reflectance infrared fourier transform spectroscopy study, *ACS Catal.* 11 (2021) 7876–7889, <https://doi.org/10.1021/acscatal.1c01981>.
- [30] Y. Ma, L. Wang, J. Ma, H. Wang, C. Zhang, H. Deng, H. He, Investigation into the enhanced catalytic oxidation of o-xylene over MOF-derived Co_3O_4 with different shapes: the role of surface twofold-coordinate lattice oxygen ($\text{O}_{2\text{f}}$), *ACS Catal.* 11 (2021) 6614–6625, <https://doi.org/10.1021/acscatal.1c01116>.
- [31] M. Qiu, Z. Chen, Z. Yang, W. Li, Y. Tian, W. Zhang, Y. Xu, H. Cheng, ZnMn_2O_4 nanorods: an effective Fenton-like heterogeneous catalyst with $t_{2g}^3e_g^1$ electronic configuration, *Catal. Sci. Technol.* 8 (2018) 2557.
- [32] N. Becknell, P.P. Lopes, T. Hatsukade, X. Zhou, Y. Liu, B. Fisher, D.Y. Chung, M. G. Kanatzidis, N.M. Markovic, S. Tepavcevic, V.R. Stamenkovic, Employing the dynamics of the electrochemical interface in aqueous zinc-ion battery cathodes, *Adv. Funct. Mater.* 31 (2021) 2102135, <https://doi.org/10.1002/adfm.202102135>.
- [33] L. Lyu, C.W. Kim, K.-D. Seong, J. Kang, S. Liu, Y. Yamauchi, Y. Piao, Defect engineering induced heterostructure of Zn-birnessite/spinel ZnMn_2O_4 nanocrystal for flexible asymmetric supercapacitor, *Chem. Eng. J.* 430 (2022), 133115, <https://doi.org/10.1016/j.cej.2021.133115>.
- [34] L. Liu, X. Gu, Y. Cao, X. Yao, L. Zhang, C. Tang, F. Gao, L. Dong, Crystal-plane effects on the catalytic properties of Au/ TiO_2 , *ACS Catal.* 3 (2013) 2768–2775, <https://doi.org/10.1021/cs400492w>.
- [35] M. Ziemba, C. Schilling, M.V. Ganduglia-Pirovano, C. Hess, Toward an atomic-level understanding of ceria-based catalysts: When experiment and theory go hand in hand, *Acc. Chem. Res.* 54 (2021) 2884–2893, <https://doi.org/10.1021/acs.accounts.1c00226>.
- [36] M. Zhang, S. Cai, J. Li, E.A. Elimian, J. Chen, H. Jia, Ternary multifunctional catalysts of polymeric carbon nitride coupled with Pt-embedded transition metal oxide to enhance light-driven photothermal catalytic degradation of VOCs, *J. Hazard. Mater.* 412 (2021), 125266, <https://doi.org/10.1016/j.jhazmat.2021.125266>.
- [37] F. Li, J. Tang, Q. Ke, Y. Guo, M.N. Ha, C. Wan, Z. Lei, J. Gu, Q. Ling, V.N. Nguyen, W. Zhan, Investigation into enhanced catalytic performance for epoxidation of styrene over $\text{LaSrCo}_x\text{Fe}_{2-x}\text{O}_6$ double perovskites: the role of singlet oxygen species promoted by the photothermal effect, *ACS Catal.* 11 (2021) 11855–11866, <https://doi.org/10.1021/acscatal.1c03164>.
- [38] F. Bi, X. Zhang, J. Chen, Y. Yang, Y. Wang, Excellent catalytic activity and water resistance of UiO-66-supported highly dispersed Pd nanoparticles for toluene catalytic oxidation, *Appl. Catal. B-Environ.* 269 (2020), 118767, <https://doi.org/10.1016/j.apcatb.2020.118767>.
- [39] Y. Xu, J. Dhainaut, J.-P. Dacquin, A.-S. Mamede, M. Marinova, J.-F. Lamonier, H. Vezin, H. Zhang, S. Royer, $\text{La}_{1-x}\text{(Sr, Na, K)}_x\text{MnO}_3$ perovskites for HCHO oxidation: the role of oxygen species on the catalytic mechanism, *Appl. Catal. B-Environ.* 287 (2021), 119955, <https://doi.org/10.1016/j.apcatb.2021.119955>.
- [40] J. Li, E. Yu, S. Cai, X. Chen, J. Chen, H. Jia, Y. Xu, Noble metal free, $\text{CeO}_2/\text{LaMnO}_3$ hybrid achieving efficient photo-thermal catalytic decomposition of volatile organic compounds under IR light, *Appl. Catal. B-Environ.* 240 (2019) 141–152, <https://doi.org/10.1016/j.apcatb.2018.08.069>.
- [41] K. Sasidharachari, K.Y. Cho, S. Yoon, Mesoporous ZnMn_2O_4 nanospheres as a nonprecious bifunctional catalyst for Zn–Air batteries, *ACS Appl. Energy Mater.* 3 (2020) 3293–3301, <https://doi.org/10.1021/acsaem.9b02294>.
- [42] H. Deng, X. Fei, Y. Yang, J. Fan, J. Yu, B. Chen, L. Zhang, S-scheme heterojunction based on p-type ZnMn_2O_4 and n-type ZnO with improved photocatalytic CO_2 reduction activity, *Chem. Eng. J.* 409 (2021), 127377, <https://doi.org/10.1016/j.cej.2020.127377>.
- [43] E. Yu, J. Li, J. Chen, Z. Hong, H. Jia, Enhanced photothermal catalytic degradation of toluene by loading Pt nanoparticles on manganese oxide: Photoactivation of lattice oxygen, *J. Hazard. Mater.* 388 (2020), 121800, <https://doi.org/10.1016/j.jhazmat.2019.121800>.
- [44] L. Lan, Z. Shi, Q. Zhang, Y. Li, Y. Yang, S. Wu, X. Zhao, Defects lead to a massive enhancement in the UV-Vis-IR driven thermocatalytic activity of Co_3O_4 mesoporous nanorods, *J. Mater. Chem. A* 6 (2018) 7194, <https://doi.org/10.1039/c8ta01362d>.
- [45] B.-S. Kim, H. Jeong, J. Bae, P.S. Kim, C.H. Kim, H. Lee, Lean NO_x trap catalysts with high low-temperature activity and hydrothermal stability, *Appl. Catal. B-Environ.* 270 (2020), 118871, <https://doi.org/10.1016/j.apcatb.2020.118871>.
- [46] M. Lu, R. Huang, W. Xu, J. Wu, M. Fu, L. Chen, D. Ye, Competitive adsorption of O_2 and toluene on the surface of $\text{FeO}_x/\text{SBA-15}$ catalyst, *Aerosol Air Qual. Res.* 17 (2017) 2310–2316, <https://doi.org/10.4209/aaqr.2016.05.0186>.
- [47] K. Wang, L. Jiang, T. Xin, Y. Li, X. Wu, G. Zhang, Single-atom V-N charge-transfer bridge on ultrathin carbon nitride for efficient photocatalytic H_2 production and

- formaldehyde oxidation under visible light, *Chem. Eng. J.* 429 (2022), 132229, <https://doi.org/10.1016/j.cej.2021.132229>.
- [48] D.A. Bulushev, S.I. Reshetnikov, L. Kiwi-Minsker, A. Renken, Deactivation kinetics of V/Ti-oxide in toluene partial oxidation, *Appl. Catal. A-Gen.* 220 (2001) 31–39, [https://doi.org/10.1016/S0926-860X\(01\)00701-3](https://doi.org/10.1016/S0926-860X(01)00701-3).
- [49] A. Airi, A. Damin, J. Xie, U. Olsbye, S. Bordiga, Catalyst sites and active species in the early stages of MTO conversion over cobalt AlPO-18 followed by IR spectroscopy, *Catal. Sci. Technol.* 12 (2022) 2775, <https://doi.org/10.1039/d2cy00303a>.
- [50] W. Qu, P. Wang, M. Gao, J.-Y. Hasegawa, Z. Shen, Q. Wang, R. Li, D. Zhang, Delocalization effect promoted the indoor air purification via directly unlocking the ring-opening pathway of toluene, *Environ. Sci. Technol.* 54 (2020) 9693–9701, <https://doi.org/10.1021/acs.est.0c02906>.
- [51] H. Sun, Z. Liu, S. Chen, X. Quan, The role of lattice oxygen on the activity and selectivity of the OMS-2 catalyst for the total oxidation of toluene, *Chem. Eng. J.* 270 (2015) 58–65, <https://doi.org/10.1016/j.cej.2015.02.017>.
- [52] J. Lu, J. Zhong, Q. Ren, J. Li, L. Song, S. Mo, M. Zhang, P. Chen, M. Fu, D. Ye, Construction of Cu-Ce interface for boosting toluene oxidation: Study of Cu-Ce interaction and intermediates identified by in situ DRIFTS, *Chin. Chem. Lett.* 32 (2021) 3435–3439, <https://doi.org/10.1016/j.ccl.2021.05.029>.
- [53] S. Besselmann, E. Löffler, M. Muhler, On the role of monomeric vanadyl species in toluene adsorption and oxidation on V₂O₅/TiO₂ catalysts: a Raman and in situ DRIFTS study, *J. Mol. Catal. A-Chem.* 162 (2000) 401–411, [https://doi.org/10.1016/S1381-1169\(00\)00307-1](https://doi.org/10.1016/S1381-1169(00)00307-1).
- [54] J. Fan, Q. Ren, S. Mo, H. Sun, M. Fu, J. Wu, L. Chen, P. Chen, D. Ye, Transient in-situ DRIFTS investigation of catalytic oxidation of toluene over α -, γ - and β -MnO₂, *ChemCatChem* 12 (2020) 1046–1054, <https://doi.org/10.1002/cctc.201901839>.
- [55] X. Zhang, F. Bi, Z. Zhu, Y. Yang, S. Zhao, J. Chen, X. Lv, Y. Wang, J. Xu, N. Liu, The promoting effect of H₂O on rod-like MnCeO_x derived from MOFs for toluene oxidation: a combined experimental and theoretical investigation, *Appl. Catal. B-Environ.* 297 (2021), 120393, <https://doi.org/10.1016/j.apcatb.2021.120393>.
- [56] P. Chen, W. Cui, H. Wang, X. Dong, J. Li, Y. Sun, Y. Zhou, Y. Zhang, F. Dong, The importance of intermediates ring-opening in preventing photocatalyst deactivation during toluene decomposition, *Appl. Catal. B-Environ.* 272 (2020), 118977, <https://doi.org/10.1016/j.apcatb.2020.118977>.
- [57] W. Qu, P. Wang, M. Gao, J.-Y. Hasegawa, Z. Shen, Q. Wang, R. Li, D. Zhang, Delocalization effect promoted the indoor air purification via directly unlocking the ring-opening pathway of toluene, *Environ. Sci. Technol.* 54 (2020) 9693–9701, <https://doi.org/10.1021/acs.est.0c02906>.